**Supplementary information**

# Observation of intrinsic chiral bound states in the continuum

**Supplementary Information for**

# Observation of intrinsic chiral bound states in the continuum

Yang Chen[1, 2†], Huachun Deng[3†], Xinbo Sha[3†], Weijin Chen[2†], Ruize Wang[1], Yuhang Chen[1], Dong Wu[1], Jiaru Chu[1], Yuri S. Kivshar[4], Shumin Xiao[3, 5]*, Cheng-Wei Qiu[2]*

*[1]Chinese Academy of Sciences Key Laboratory of Mechanical Behavior and Design of Materials, Department of Precision Machinery and Precision Instrumentation, University of Science and Technology of China, 230027 Hefei, China*

*[2]Department of Electrical and Computer Engineering, National University of Singapore, 117583 Singapore, Singapore*

*[3]Ministry of Industry and Information Technology Key Lab of Micro-Nano Optoelectronic Information System, Harbin Institute of Technology, Shenzhen, 518055, P. R. China*

*[4]Nonlinear Physics Center, Research School of Physics, Australian National University, Canberra, ACT2601, Australia*

*[5]Pengcheng Laboratory, Shenzhen, 518055, P. R. China*


*†These authors contributed equally: Yang Chen, Huachun Deng, Xinbo Sha and Weijin Chen*

*\*Email: shumin.xiao@hit.edu.cn, chengwei.qiu@nus.edu.sg;*

**Section 1. Mode profiles of quasi-BICs**

**Section 2. Proof that the near-field of BIC is linearly polarized**

**Section 3. Realizing chiral BIC in TE$_1$ mode**

**Section 4. The role played by the PMMA layer**

**Section 5. Fabrication details of the slant-perturbation metasurface**

**Section 6. Details of the optical characterization setup**

**Section 7. Measured reflection spectra for different slant angles**

**Section 8. Theoretical prediction of $\sqrt{A}$**

**Section 9. Limits connecting the $Q$-factor and CD of chiral BIC**

**Section 10. Dependence of optical chirality on the azimuthal angle of rotation**

**Section 11. Electric near-field distributions of the chiral BIC**

**Section 12. Measured transmission spectra data**

**Section 13. Comparison between intrinsic chiral BIC and quasi-BIC with false chirality**

# Section 1. Mode profiles of quasi-BICs
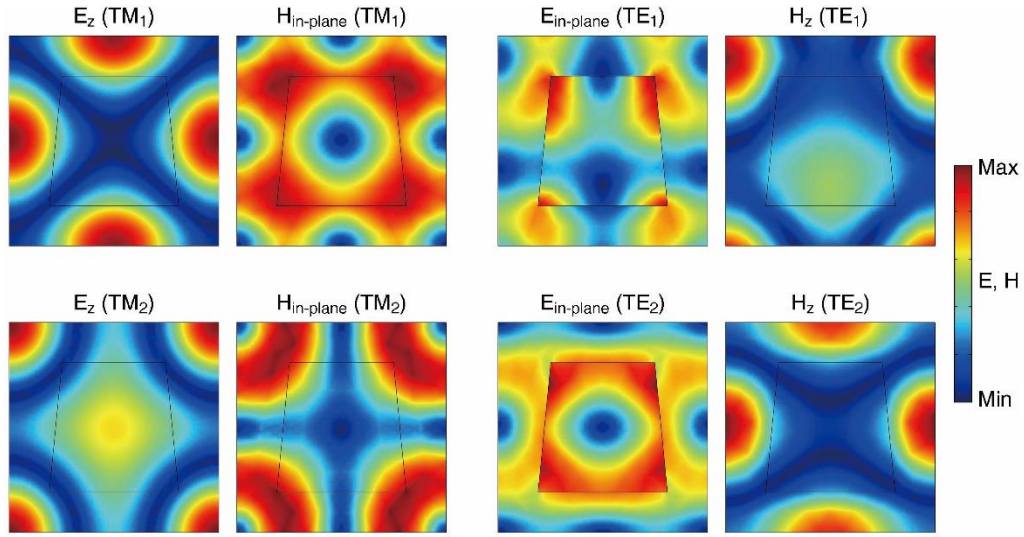


**Supplementary Fig. 1 | Mode profiles of the quasi-BICs of different bands.** Electric and magnetic field distributions of the quasi-BICs of different Bloch modes are plotted on the central *x-y* plane of the nanohole. Accordingly, those Bloch modes are classified into transverse-magnetic-like (TM) and transverse-electric-like (TE) mode.

# Section 2. Proof that the near-field of BIC is linearly polarized
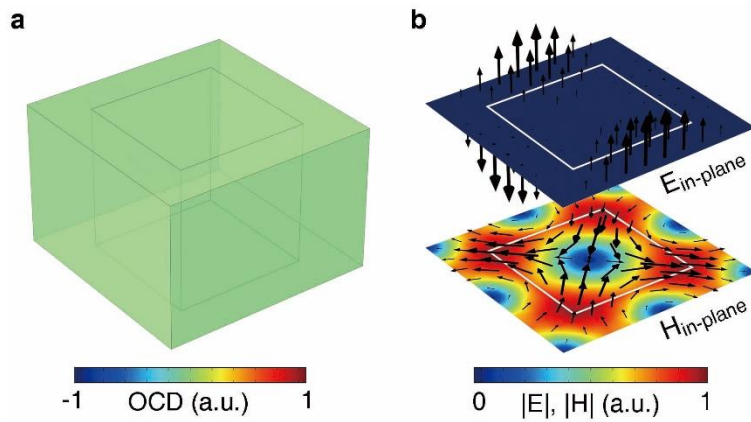


**Supplementary Fig. 2 | Mode profiles of BIC. a,** Volume OCD distributions of the BIC. **b,** In-plane components of electric ($E_{in-plane}$) and magnetic ($H_{in-plane}$) field distributions at the central *x-y* plane of the metasurface without perturbations.

Let $E$ be the electric field of an eigenmode of the master operator $\bar{H} = \frac{1}{\varepsilon}\nabla\times\nabla\times$, i.e., $\bar{H}E = \omega E$.

As the master operator satisfies the time-reversal symmetry: $T^{-1}\bar{H}T = \bar{H}$, we could obtain corresponding equation of the electric field $\bar{H}TE = T(\omega E)$. If the mode is BIC, that is, the imaginary part of its eigenfrequency is zero, then $\bar{H}TE = \omega T(E) = \omega T(E)$. Therefore, there are two electric fields $E$ and $T(E)$ that are associated with the same eigenfrequency $\omega$. These two fields must equal to each other as: $TE = E^* = E$, which means the imaginary part of the electric field is zero. We could obtain a similar conclusion for magnetic fields. Therefore, the electric field and magnetic field of BIC is linear polarized. The OCD distribution is zero over the structure (Supplementary Fig. 2a). Besides, the electromagnetic field distributions cancel each other to prohibit the far-field coupling (Supplementary Fig. 2b).

## Section 3. Realizing chiral BIC in TE₁ mode
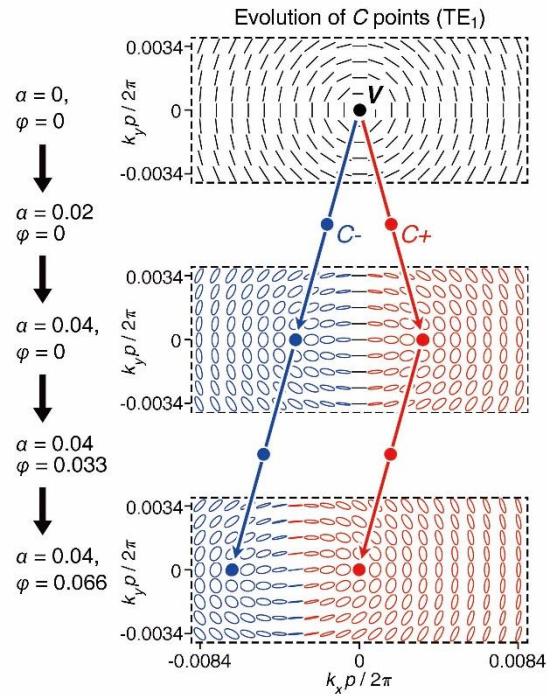


**Supplementary Fig. 3 | Realizing chiral BIC in TE₁ mode.** Momentum-space evolution of the C points of

TE$_1$ mode for different $\alpha$ and $\varphi$. The C+ and C- points are generated and separated by increased $\alpha$, and then simultaneously shifted to the left by increased $\varphi$. Intrinsic chiral BIC is realized for the case of $\alpha = 0.04$ and $\varphi$ = 0.066.

## Section 4. The role played by the PMMA layer
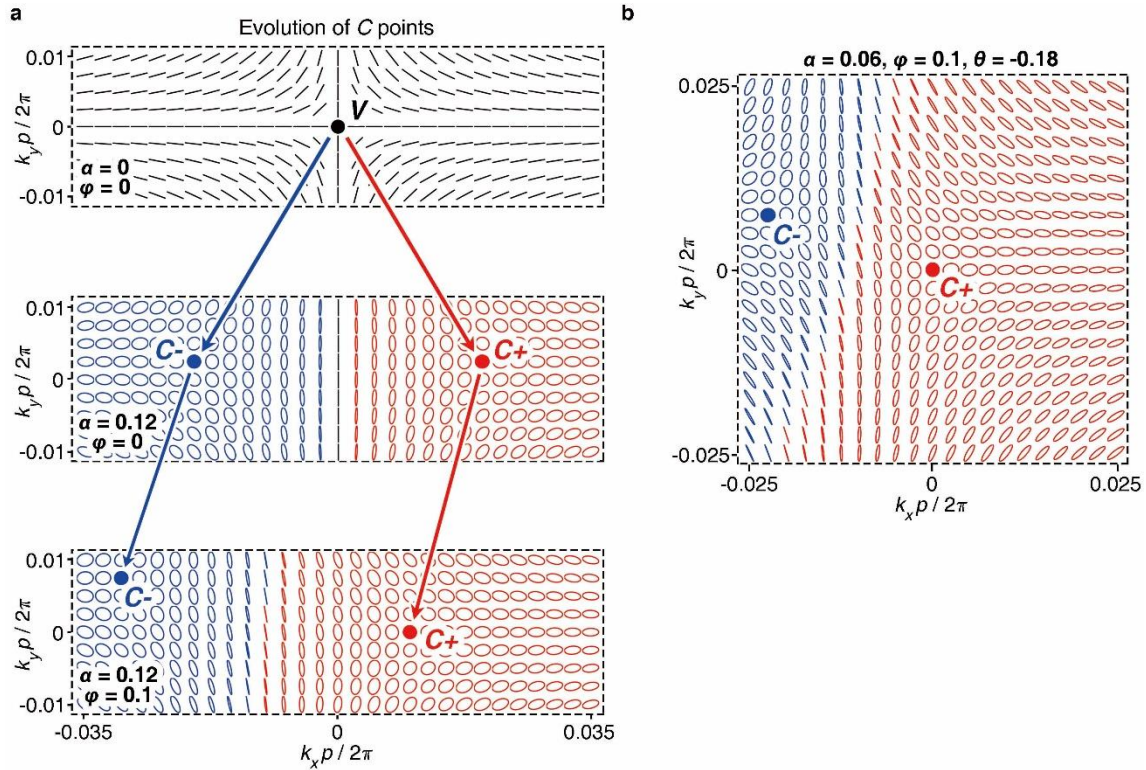


**Supplementary Fig. 4 | Analysis of the role played by the PMMA layer. a,** Evolution of C points over $k$-space for the metasurfaces without the PMMA layer for different $\alpha$ and $\varphi$. The elliptical polarizations are represented by ellipses of red or blue colors corresponding to right- or left-handed states, while the black lines represent linear polarizations. Using the same parameters as in the main text, the C+ point cannot be moved back to the $\Gamma$ point. **b,** Achieving intrinsic chiral BIC of the slant-perturbation metasurface without the PMMA layer by introducing an addition perturbation parameter $\theta$ as defined in Supplementary Fig. 11.

In the simulations and experiments of the main context, a layer of PMMA is covered over the TiO$_2$ metasurface to match the refractive index of the silica substrate and guarantee a homogenous environment for the TiO$_2$ nanostructures. In this section, we will discuss the case without PMMA layer. As shown in Supplementary Fig. 4a, when no perturbations are introduced

($\alpha$ = 0, $\varphi$ = 0), a BIC is present at the $\Gamma$ point of Brillouin Zone for the TM$_1$ mode due to the $C_2^z$ symmetry of the structure, and the polarization map is similar to the case with PMMA. When an in-plane perturbation is induced ($\alpha$ = 0.12, $\varphi$ = 0), a pair of C points are generated, and they are farther away from the $\Gamma$ point ($k_xp/2\pi$ = ±0.02) compared to the case with PMMA ($k_xp/2\pi$ = ±0.01). If we use the same combination of perturbations as the case with PMMA ($\alpha$ = 0.12, $\varphi$ = 0.1), no C point can be moved back to the $\Gamma$ point, because in this case the out-of-plane mirror symmetry is broken not only by the slant TiO$_2$ holes, but also by the different environmental indices above and below the TiO$_2$ slab. Besides, due to the unbalanced field distributions on the top and bottom of the TiO$_2$ slab, the introduction of in-plane and out-of-plane perturbations will both move C points in $k_y$ direction. Thus, an additional perturbation of the azimuthal angle of slant $\theta$ is required to move a C point back to the $\Gamma$ point. In **Supplementary Fig. 4b**, we showcase the achievement of intrinsic chiral BIC through the cooperative perturbations of $\alpha$ = 0.06, $\varphi$ = 0.1 and $\theta$ = -0.18. Apparently, it is more complicated, especially for fabrication, to realize chiral BIC for the case without PMMA.

**Section 5. Fabrication details of the slant-perturbation metasurface**
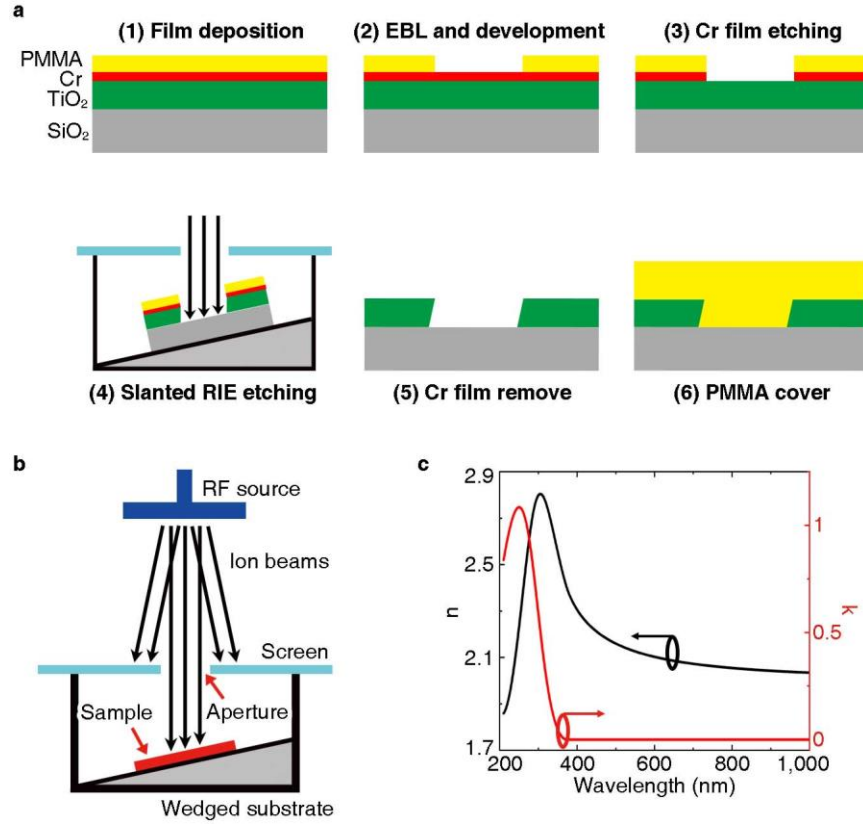
**Supplementary Fig. 5 | Fabrication details. a,** Schematic of the fabrication process. **b,** Schematic illustration of the slanted RIE system. An aperture diameter of 3 mm is taken as a good balance between the uniformity of sidewall tilting and the etching rate. **c,** Measured refractive index of the evaporated $TiO_2$ film. The absorption coefficient $k$ is negligibly small for the wavelength range longer than 400 nm, which is important for suppressing the non-radiative loss of slant-perturbation metasurfaces.
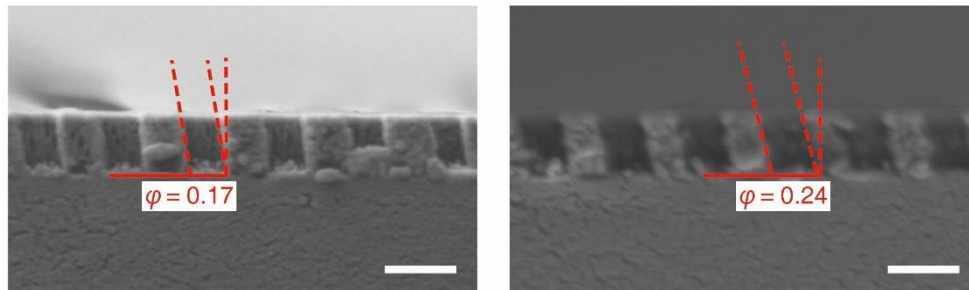


**Supplementary Fig. 6 | Cross-sectional SEM images of fabricated metasurfaces with different slant angles.** The slant angles are 0.17 rad (left) and 0.24 rad (right). Scale bar: 300 nm. By checking over the sample, the uniformity of the etch process is good across the 200 μm sample. The main obstacle for further

enlarging the sample size is the capacity of EBL. When fabricating a larger sample, the pattern is divided into multiple sub-areas to be exposed separately, which are then combined together. Alignment dislocation will be inevitably generated on the boundaries.

## Section 6. Details of the optical characterization setup
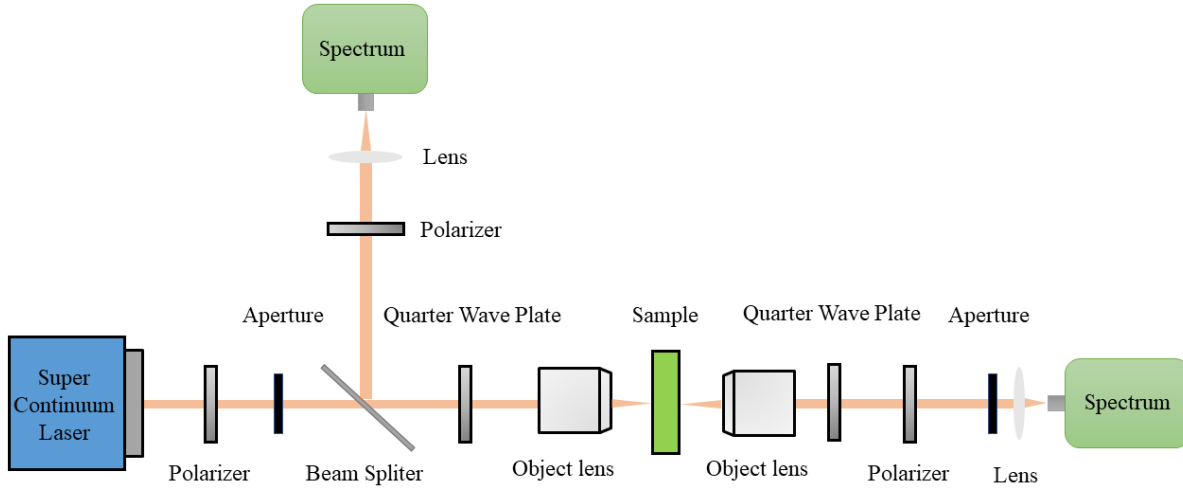


**Supplementary Fig. 7 | Schematic diagram of the optical setup for measuring the transmission and reflection spectra.**

## Section 7. Measured reflection spectra for different slant angles
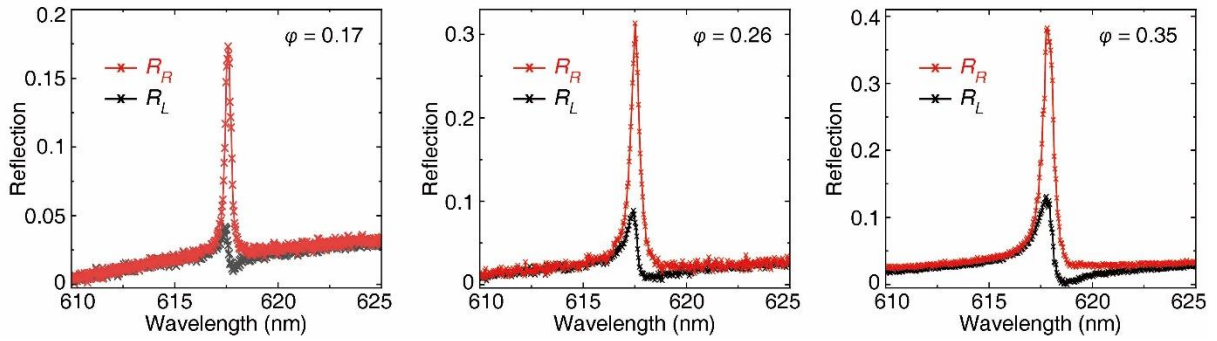


**Supplementary Fig. 8 | Measured reflection spectra for different slant angles $\varphi$.** The in-plane perturbation $\alpha$ is fixed as 0.12, and the retrieved CD values correspond to the data points in Fig. 3b of the main text.

## Section 8. Theoretical prediction of $\sqrt{A}$
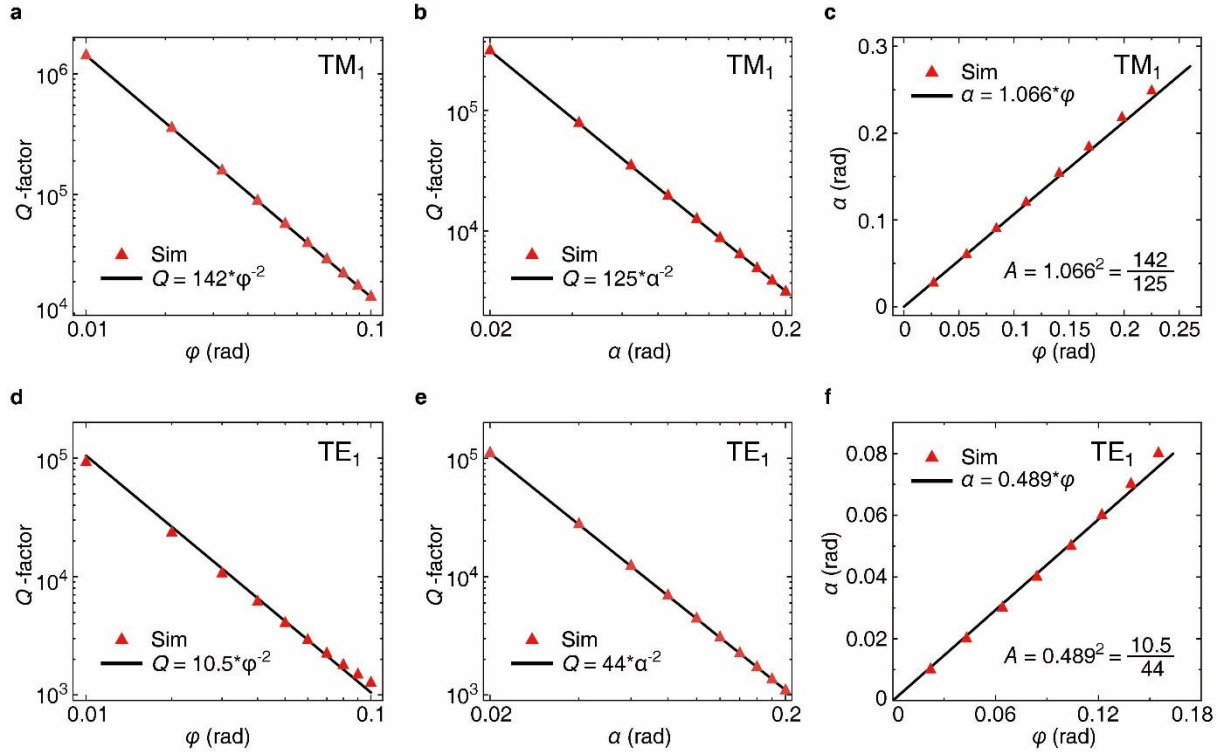
**Supplementary Fig. 9 | Theoretical prediction of the slope $\sqrt{A}$. a, b,** Simulated and theoretical dependence of $Q$-factors on **(a)** $\varphi$ and **(b)** $\alpha$ for the TM$_1$ quasi-BIC. **c,** Simulated and theoretically predicted relation between $\varphi$ and $\alpha$ for maximizing CD. The slope $\sqrt{A}$ is calculated based on **(a)** and **(b)**. **d, e,** Simulated and theoretical dependence of $Q$-factors on **(d)** $\varphi$ and **(e)** $\alpha$ for the TE$_1$ quasi-BIC. **f,** Simulated and theoretically predicted relation between $\varphi$ and $\alpha$ for maximizing CD. The slope $\sqrt{A}$ is calculated based on **(d)** and **(e)**.

Guided by the physics of BIC, its $Q$-factor approximately follows an inversely quadratic law of asymmetric perturbations. This relation is verified by simulation results in Supplementary Fig. 9a and b. The scale factors of TM$_1$ quasi-BIC are retrieved to be 142 and 125 for $\varphi$ and $\alpha$, respectively. As a result, the parameter A in the equation $Q \sim 1/(\alpha^2 + A\varphi^2)$ is calculated to be A = 142/125 = 1.136. Then, $\varphi$ and $\alpha$ should follow a linear relationship of $\alpha = \sqrt{A} \cdot \varphi = 1.066 \cdot \varphi$ to maximize CD according to the main text. This theoretical prediction is confirmed by simulation results in Supplementary Fig. 9c. In the same way, we have also retrieved the scale factors of TE$_1$ quasi-BIC for $\varphi$ and $\alpha$ in Supplementary Fig. 9d and e. The corresponding A is calculated to be 0.239, and the linear relationship between $\varphi$ and $\alpha$ is confirmed again for TE$_1$

quasi-BIC in Supplementary Fig. 9f. We can see that the parameter A takes different values for TM$_1$ and TE$_1$ quasi-BICs, which is believed to be related to their respective mode profiles.

## Section 9. Limits connecting the $Q$-factor and CD of chiral BIC
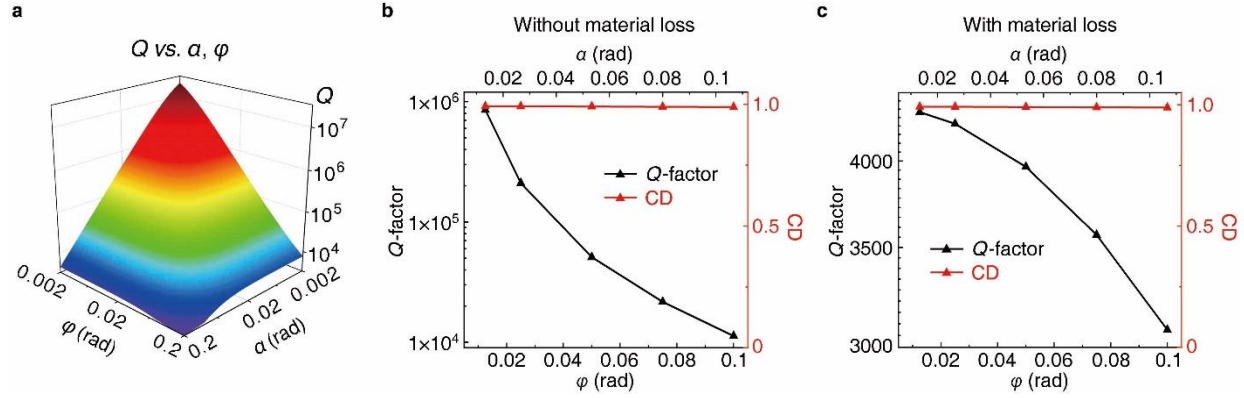


**Supplementary Fig. 10 | Inherent limit connecting $Q$ and CD.** Simulated $Q$-factor (in log scale) and CD of the TM$_1$ chiral BIC as functions of the cooperative change of perturbations $\alpha$ and $\varphi$ for the case **(a)** without and **(b)** with material loss.

As is well studied[1], the introduction of perturbations will cause a significant decrease of $Q$-factors for quasi-BICs, which approximately obey an inverse quadratic law with respect to $\alpha$ and $\varphi$ (Supplementary Fig. 10a). Here, we will discuss the inherent limit between the $Q$-factor and CD of chiral BIC. According to the main text, as long as the two perturbations $\alpha$ and $\varphi$ are changed cooperatively, approximately following the linear relationship described before, the state of intrinsic chiral BIC can be maintained and thus the amplitude of CD is kept to the maximum of unity (Supplementary Fig. 10b and c). As to the evolution of $Q$-factor, the situation can be different for the case with and without material loss. If material loss is absent, the $Q$-factor will approximately obey an inverse quadratic law with respect to the cooperative decrease of $\alpha$ and $\varphi$ (Supplementary Fig. 10b). In theory, there is no limit for the achievable $Q$-factor as long as $\alpha$ and $\varphi$ can be accurately controlled to arbitrarily small values. But for the case with material loss, the increase of $Q$-factor with reducing $\alpha$ and $\varphi$ is much slower (Supplementary Fig. 10c), especially when $\alpha$ and $\varphi$ are small. This is because the total $Q$-factor of chiral BIC can be divided into a radiative component $Q_{rad}$ and a non-radiative component

$Q_{nrad}$, following the equation $1/Q_{BIC} = 1/Q_{rad} + 1/Q_{nrad}$. The reduction of geometric perturbations can only increase the radiative $Q_{rad}$, while the nonradiative $Q_{nrad}$ sets an upper limit for the total $Q$-factor of chiral BIC. We have to point out that the influence of material loss is always present in experiments. Besides, the accessible fabrication capacity, including sample size, uniformity and roughness, can also seriously deteriorate the obtained $Q$-factor.

## Section 10. Dependence of optical chirality on the azimuthal angle of rotation
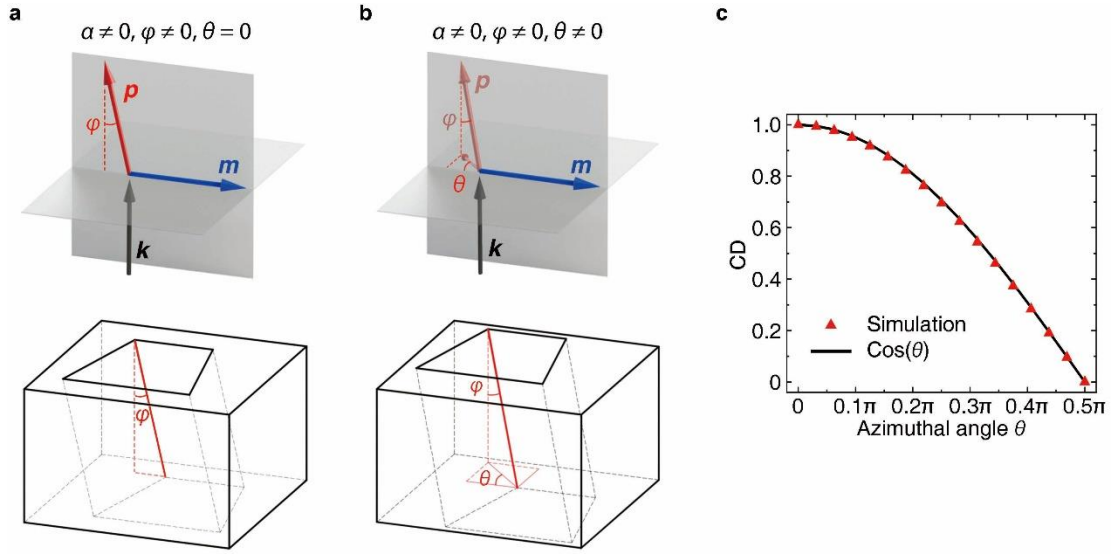


**Supplementary Fig. 11 | Optical chirality of chiral BIC as a function of azimuthal angle $\theta$. a, b,** Schematics of the slant-perturbation metasurface **(a)** without and **(b)** with a non-zero azimuthal angle of rotation $\theta$. Their corresponding configurations of electric dipole $p$, magnetic dipole $m$ and incident wavevector $k$ are shown on the top. **c,** Simulated CDs of the chiral BICs as a function of azimuthal angle $\theta$.

In the main text, the nanohole is slanted along $x$-direction, so that the mirror symmetries of $x$-$y$ and $y$-$z$ planes are simultaneously broken. In factor, there is another degree of freedom, i.e., the azimuthal angle of rotation $\theta$, that determines the slant direction in $x$-$y$ plane. Schematics of metasurfaces without and with a nonzero $\theta$ are shown in Supplementary Fig. 11a and b for comparison. Correspondingly, the Eq. 2 in the main text can be rewritten as:

$$CD \sim p_\perp \cdot m_\perp = |p||m| \sin(\varphi) \cos(\theta) \sim \frac{\sin(\varphi)\cos(\theta)}{\alpha^2 + A\varphi^2}, \qquad (1)$$

Thus, the dependence of CD on $\theta$ is anticipated to follow a cosine function, which is confirmed by simulation results (Supplementary Fig. 11c)

## Section 11. Electric near-field distributions of the chiral BIC
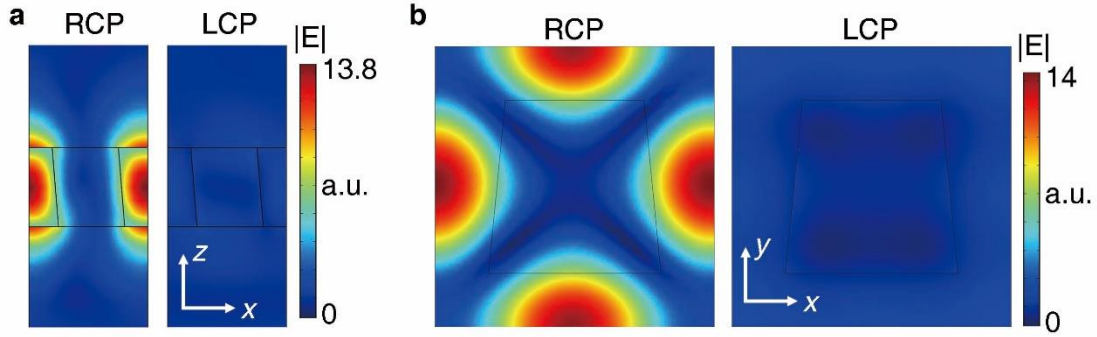


**Supplementary Fig. 12 | Electric near-field distributions of the chiral BIC. a, b,** Electric near-field distributions of the metasurface under RCP and LCP incidence at the resonance wavelength of $TM_1$ chiral BIC retrieved from the **(a)** x-z and **(b)** x-y plane. As demonstrated, the chiral BIC strongly couples with RCP incidence generating highly enhanced near-field distributions, while it is decoupled from LCP incidence.

## Section 12. Measured transmission spectra data
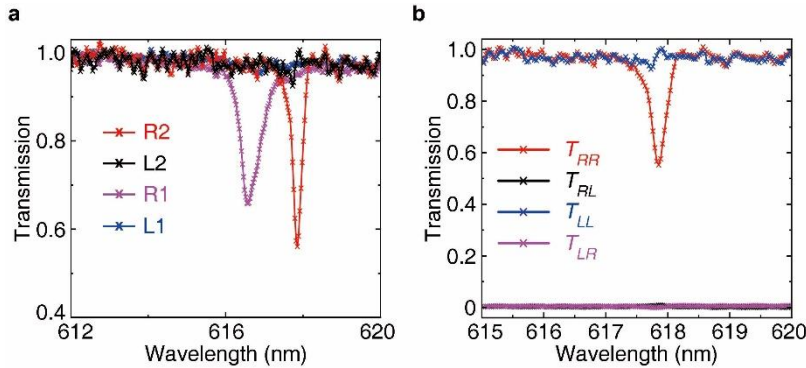


**Supplementary Fig. 13 | Measured transmission spectra. a,** Measured transmission spectra of the two metasurface samples of 68 μm (L1 & R1) and 200 μm sizes (L2 & R2) under LCP and RCP incidence. **b,** Measured transmission matrix $T$ in the circular basis for the 200 μm sample, confirming the absence of polarization conversion.

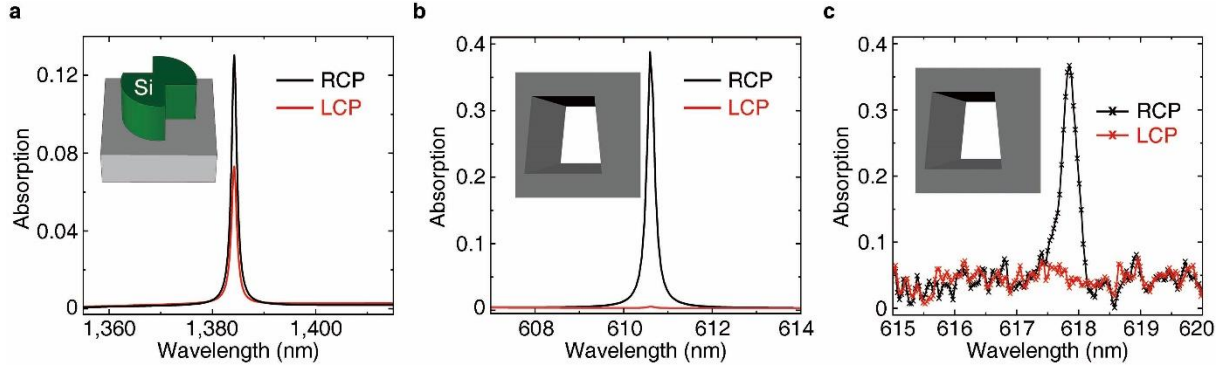## Section 13. Comparison between intrinsic chiral BIC and quasi-BIC with false chirality
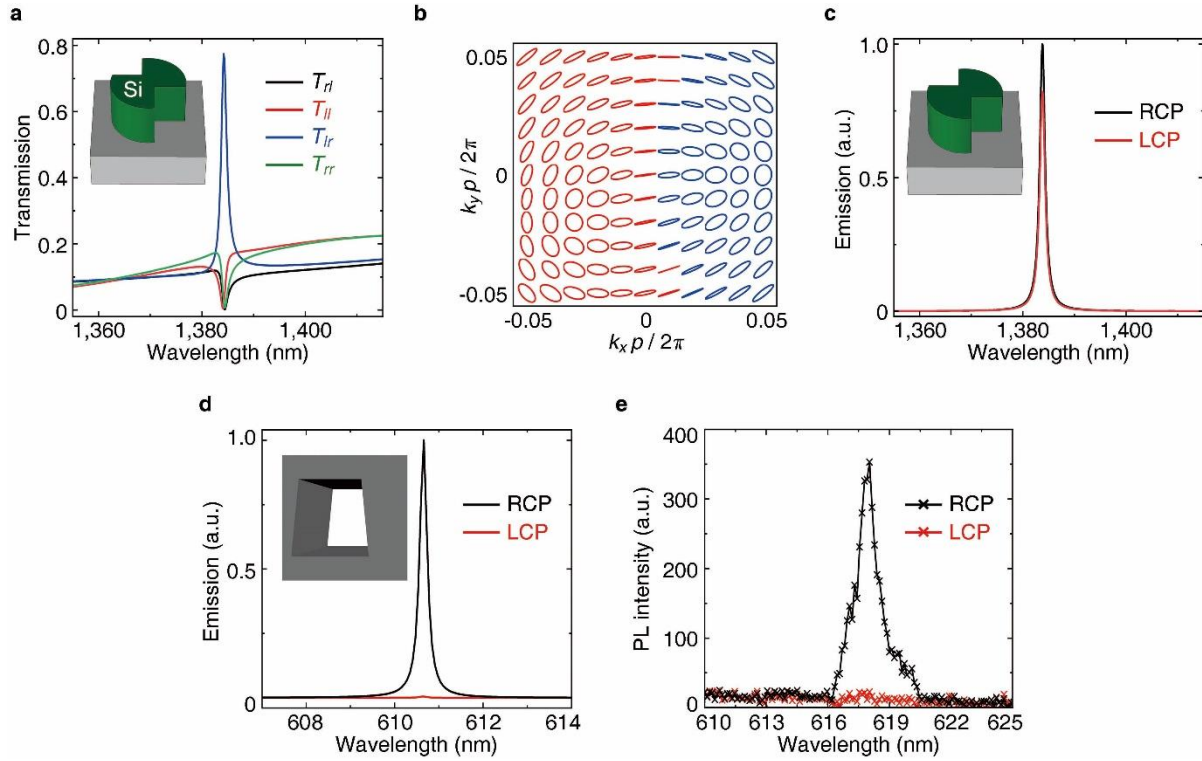
**Supplementary Fig. 14 | Difference between intrinsic chiral BIC and quasi-BIC with false chirality in chiral emission. a,** Simulated transmission matrix $T$ of the anisotropic silicon metasurface showing strong CD signals as a result of polarization conversion. **b,** Eigenpolarization map of the silicon metasurface. The elliptical polarizations are represented by ellipses of red or blue colors corresponding to right- or left-handed states. c, Simulated emission spectra of the silicon metasurface excited by a local electric dipole. **d,** Simulated emission spectra of our proposed slant-perturbation metasurface excited by a local electric dipole. **e,** Measured PL emission spectra of dye molecules when coupled to the slant-perturbation metasurface.

Chiral emission is one typical and important application of high-$Q$ chiral resonances. The proposal of chiral BIC has been widely anticipated to unleash great potentials in this area, because its intrinsic chirality can modulate the helicity of emission while its high $Q$-factor can significantly enhance the emission rate of associated emitters, such as quantum dots, halide perovskites and GaAs. Also, the investigation of chiral emission can clarify the fundamental difference between intrinsic chiral BIC and other BIC works relying on false chirality that

generates large CDs. As one benchmark, we adopted the structural design from the reference[2]. Helicity-resolved transmission spectra under normal incidence are simulated in Supplementary Fig. 14a, where $T_{lr}$ denotes the transmission of LCP component under the incidence of RCP light. Although the CD in transmission is large, the dominant component $T_{lr}$ is produced by polarization conversion, implying that the acquired CD is not originated from the intrinsic chirality of the quasi-BIC but from anisotropy-induced polarization conversion. By checking the momentum-space eigenpolarization map of the quasi-BIC (Supplementary Fig. 14b), it is also clear that the eigenpolarization at $\Gamma$ point is close to linear polarization possessing a small ellipticity angle of only 0.044 rad. By putting an electric dipole inside the structure, we obtain the helicity-resolved emission spectra in Supplementary Fig. 14c, where the degree of circular polarization (DCP) of the emission calculated by DCP = $(I_{RCP} - I_{LCP}) / (I_{RCP} + I_{LCP})$ is only 0.097, where $I_{RCP}$ and $I_{LCP}$ are the intensities of RCP and LCP emission. We note that such a weak DCP is generated by the different refractive indices above and below the silicon structure, but not attributed to the structural asymmetry of the silicon nanostructure.

In contrast, if an electric dipole is positioned inside our proposed slanted metasurface to excite the intrinsic chiral BIC, the acquired DCP of emission is nearly unity, indicating a high purity of chiral emission (Supplementary Fig. 14d). In this regard, we performed new experiments by spin-coating dye molecules on the slant-perturbation metasurface, which are pumped by a 400 nm CW laser. The emission band of the dye molecules spectrally matches with the resonant wavelength of the chiral BIC, and the measured photoluminescence (PL) spectrum exhibits CD as large as 0.9. The emission peak of RCP PL is very sharp due to the high $Q$-factor of chiral BIC, while no emission peak is observed for LCP PL because of the intrinsic chirality of chiral BIC (Supplementary Fig. 14e). According to the chiral emission results, intrinsic chiral BIC with true chirality is fundamentally distinct from those BIC states with false chirality[2-4].

**Supplementary Fig. 15 | Difference between intrinsic chiral BIC and quasi-BIC with false chirality in chiral absorption. a,** Simulated absorption spectra of the anisotropic silicon metasurface showing a limited difference between RCP and LCP incidence. **b, c,** Helicity-resolved absorption spectra of our proposed slant-perturbation metasurface retrieved by **(b)** simulations and **(c)** experiments.

Helicity-dependent absorption is another basic feature of high-$Q$ chiral resonances, which can be harnessed for polarized photodetectors, photovoltaic, etc. Moreover, we note that although the concept of CD is widely utilized for differential transmission, reflection, absorption or scattering nowadays, its original definition is associated with the helicity-dependent absorption[5]. Thus, the investigation of helicity-dependent absorption can help further reveal the fundamental difference between quasi-BICs with true chirality and false chirality. Using the same structure as the reference[2], we simulate the absorption under RCP and LCP normal incidence (Supplementary Fig. 15a), and the retrieved CD is only 0.28. We can see that although this structure can exhibit large CD in transmission, the chirality of the quasi-BIC is limited, exhibiting small CD in absorption. In contrast, our proposed slanted metasurfaces exhibits a near-unity CD in absorption (Supplementary Fig. 15b and c), implying that the structure is completely transparent for the LCP incidence.

## Supplementary References

1.   Koshelev K, Lepeshov S, Liu M, Bogdanov A, Kivshar Y. Asymmetric Metasurfaces with

High-Q Resonances Governed by Bound States in the Continuum. *Phys Rev Lett* **121,** 193903 (2018).

2.   Shi T, Deng ZL, Geng G, Zeng X, Zeng Y, Hu G*, et al.* Planar chiral metasurfaces with maximal and tunable chiroptical response driven by bound states in the continuum. *Nat Commun* **13,** 4111 (2022).

3.   Liu W, Wang B, Zhang Y, Wang J, Zhao M, Guan F*, et al.* Circularly Polarized States Spawning from Bound States in the Continuum. *Phys Rev Lett* **123,** 116104 (2019).

4.   Wu J, Xu X, Su X, Zhao S, Wu C, Sun Y*, et al.* Observation of Giant Extrinsic Chirality Empowered by Quasi-Bound States in the Continuum. *Physical Review Applied* **16,** 064018 (2021).

5.   Barron LD. *Molecular light scattering and optical activity* (Cambridge University Press, Cambridge, 2004).